



**Journal of
Mechanics of
Materials and Structures**

PERIDYNAMICS FOR ANTIPLANE SHEAR AND TORSIONAL DEFORMATIONS

Selda Oterkus and Erdogan Madenci

Volume 10, No. 2

March 2015



PERIDYNAMICS FOR ANTIPLANE SHEAR AND TORSIONAL DEFORMATIONS

SELDA OTERKUS AND ERDOGAN MADENCI

A rod or beam is one of the most widely used members in engineering construction. Such members must be properly designed to resist the applied loads. When subjected to antiplane (longitudinal) shear and torsional loading, homogeneous, isotropic, and elastic materials are governed by the Laplace equation in two dimensions under the assumptions of classical continuum mechanics, and are considerably easier to solve than their three-dimensional counterparts. However, when using the finite element method in conjunction with linear elastic fracture mechanics, crack nucleation and its growth still pose computational challenges, even under such simple loading conditions. This difficulty is mainly due to the mathematical structure of its governing equations, which are based on the local classical continuum theory. However, the nonlocal peridynamic theory is free of these challenges because its governing equations do not contain any spatial derivatives of the displacement components, and thus are valid everywhere in the material. This study presents the peridynamic equation of motion for antiplane shear and torsional deformations, as well as the peridynamic material parameters. After establishing the validity of this equation, solutions for specific components that are weakened by deep edge cracks and internal cracks are presented.

1. Introduction

Prediction of structural failure loads due to crack nucleation and propagation is still a challenging area of solid mechanics. Many different techniques are proposed and widely used within the scope of classical continuum mechanics. The traditional approaches to predict failure usually employ concepts from linear elastic fracture mechanics (LEFM). The major drawback of LEFM is the requirement of a preexisting initial crack in the structure. Hence, it is not capable of predicting crack nucleation. Furthermore, the mathematical formulation results in unphysical (singular) stress values at the crack tips. To overcome these problems, cohesive zone models (CZM) and extended finite element methods (XFEM) are widely accepted as an alternative and implemented in the commercially available finite element analysis programs.

Although relatively new, peridynamics (PD), introduced by Silling [2000] by reformulating the classical continuum mechanics equations, is very suitable for failure analysis of structures because it allows cracks to grow naturally without resorting to external crack growth laws. PD is based on integrodifferential equations as opposed to the partial differential equations of classical continuum mechanics. An extensive literature survey on peridynamics is given by Madenci and Oterkus [2014]. A comparison study between peridynamics, CZM, and XFEM techniques by Agwai et al. [2011] highlights the capability of the PD theory. They showed that the crack speeds obtained from all three approaches are of the same order; however, the fracture paths obtained through the PD theory are much closer to the experimental results than those of the other two techniques.

Keywords: peridynamics, nonlocal, antiplane shear, torsion, fracture.

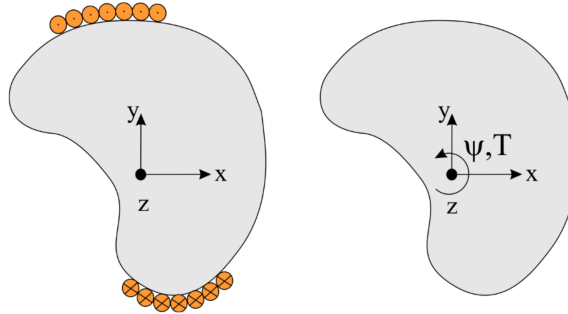


Figure 1. A beam under (left) antiplane shear and (right) torsion.

The numerical simulation of three-dimensional structures can be computationally costly. Although all structures are three-dimensional in nature, they can be idealized under certain assumptions. Under such idealization, a rod or a beam subjected to antiplane (longitudinal) shear and torsional loading can be analyzed in two dimensions. However, the PD equation of motion and the PD material parameter must reflect these idealizations. In connection to Linear Elastic Fracture Mechanics (LEFM), Lipton [2014] investigated Mode III fracture in the context of antiplane shear deformation.

As shown in Figure 1, this study presents the derivation of the PD equation of motion for antiplane shear and torsional deformations of beams with arbitrary cross-sections along with the implementation of boundary conditions. Also, it describes the determination of peridynamic material parameter in terms of shear modulus, and critical stretch in terms of critical energy release rate for tearing mode. After establishing its validity by comparing against benchmark solutions, a study of components that are weakened by deep edge cracks and internal cracks is presented.

In multiphysics analysis, many the field equations concern the solution of diffusion equation. This study also provides the framework to consider such equations with defects and stationary or moving dissimilar material interface. The partial differential equations of the classical theory cannot be applied directly to defects. This incompatibility has led to a variety of patches in the finite element method. They are entirely unnecessary with peridynamics.

2. Kinematics for antiplane shear and torsional deformation

Due to the nature of loading and the geometry of the components, the deformation of the cross-section on the z -plane is dependent only on the x - and y -coordinates. Also, the cross-section of the component remains uniform. At any instant of time, every point in the material denotes the location of a material particle, and these infinitely many material points (particles) constitute the continuum. In the undeformed state of the body, each material point is identified by its coordinates, $\mathbf{x}_{(k)}$ with $(k = 1, 2, \dots, \infty)$, and is associated with an incremental volume, $V_{(k)}$, and a mass density of $\rho(\mathbf{x}_{(k)})$. Each material point can be subjected to prescribed body loads, displacement, or velocity, resulting in motion and deformation.

According to the PD theory introduced by Silling [2000], the motion of a body is analyzed by considering the interaction of a material point, $\mathbf{x}_{(k)}$, with the other, possibly infinitely many, material points, $\mathbf{x}_{(j)}$, with $(j = 1, 2, \dots, \infty)$, in the body. Therefore, an infinite number of interactions may exist between the material point at location $\mathbf{x}_{(k)}$ and other material points. However, the influence of the material points

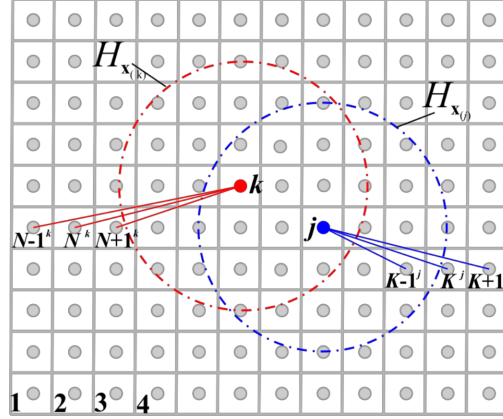


Figure 2. Peridynamic material points and their interaction with each other.

interacting with $\mathbf{x}_{(k)}$ is assumed to vanish beyond a local region (horizon), denoted by $H_{\mathbf{x}_{(k)}}$, shown in Figure 2. Similarly, the material point $\mathbf{x}_{(j)}$ interacts with the other material points in its own family, $H_{\mathbf{x}_{(j)}}$. The range of the material point $\mathbf{x}_{(k)}$ is defined by δ , referred to as the “horizon.” Also, the material points within a distance δ of $\mathbf{x}_{(k)}$ are called the family of $\mathbf{x}_{(k)}$, $H_{\mathbf{x}_{(k)}}$. The interaction of material points is prescribed through the micropotentials that depend on the deformation and constitutive properties of the material.

As shown in Figure 2, material point $\mathbf{x}_{(k)}$ interacts with its family of material points, $H_{\mathbf{x}_{(k)}}$, and is influenced by the collective deformation of all these material points. Similarly, the material point $\mathbf{x}_{(j)}$ is influenced by deformation of the material points, $H_{\mathbf{x}_{(j)}}$, in its own family. In Figure 2, the material points, $\mathbf{x}_{(k)}$ and $\mathbf{x}_{(j)}$ associated with designated as N^k and K^j with N and K denoting the sequence of material points in the domain.

With respect to a Cartesian coordinate system, the material point $\mathbf{x}_{(k)}^T = \{x_{(k)}, y_{(k)}, z_{(k)}\}$ experiences displacement, $\mathbf{u}_{(k)}^T = \{u_{(k)}, v_{(k)}, w_{(k)}\}$, and its location is described by the position vector $\mathbf{y}_{(k)} = \mathbf{x}_{(k)} + \mathbf{u}_{(k)}$ in the deformed state, as shown in Figure 3. The body load vector at material point $\mathbf{x}_{(k)}$ is represented by $\mathbf{b}_{(k)}^T = \{0, 0, b_{z(k)}\}$, respectively. The motion of a material point conforms to the Lagrangian description. In the deformed configuration, the material points $\mathbf{x}_{(k)}$ and $\mathbf{x}_{(j)}$ experience displacements $\mathbf{u}_{(k)}$ and $\mathbf{u}_{(j)}$, respectively. Their initial relative position vector $(\mathbf{x}_{(j)} - \mathbf{x}_{(k)})$ prior to deformation becomes $(\mathbf{y}_{(j)} - \mathbf{y}_{(k)})$ after deformation.

Under antiplane and torsional loadings, the initial position of material points $\mathbf{x}_{(j)}$ and $\mathbf{x}_{(k)}$ for $z = z_{(j)} = z_{(k)}$ can be defined as $\mathbf{x}_{(j)}^T = \{x_{(j)}, y_{(j)}, z\}$ and $\mathbf{x}_{(k)}^T = \{x_{(k)}, y_{(k)}, z\}$. Their initial relative position can then be expressed as

$$(\mathbf{x}_{(j)}^T - \mathbf{x}_{(k)}^T) = \{(x_{(j)} - x_{(k)}), (y_{(j)} - y_{(k)}), 0\}. \quad (1)$$

For antiplane shear deformation, these material points experience the displacements $\mathbf{u}_{(j)}^T = \{0, 0, u_{z(j)}\}$ and $\mathbf{u}_{(k)}^T = \{0, 0, u_{z(k)}\}$. Their relative position in the deformed state becomes

$$\mathbf{y}_{(j)} - \mathbf{y}_{(k)} = \mathbf{x}_{(j)} - \mathbf{x}_{(k)} + (u_{z(j)} - u_{z(k)})\mathbf{e}_z. \quad (2)$$

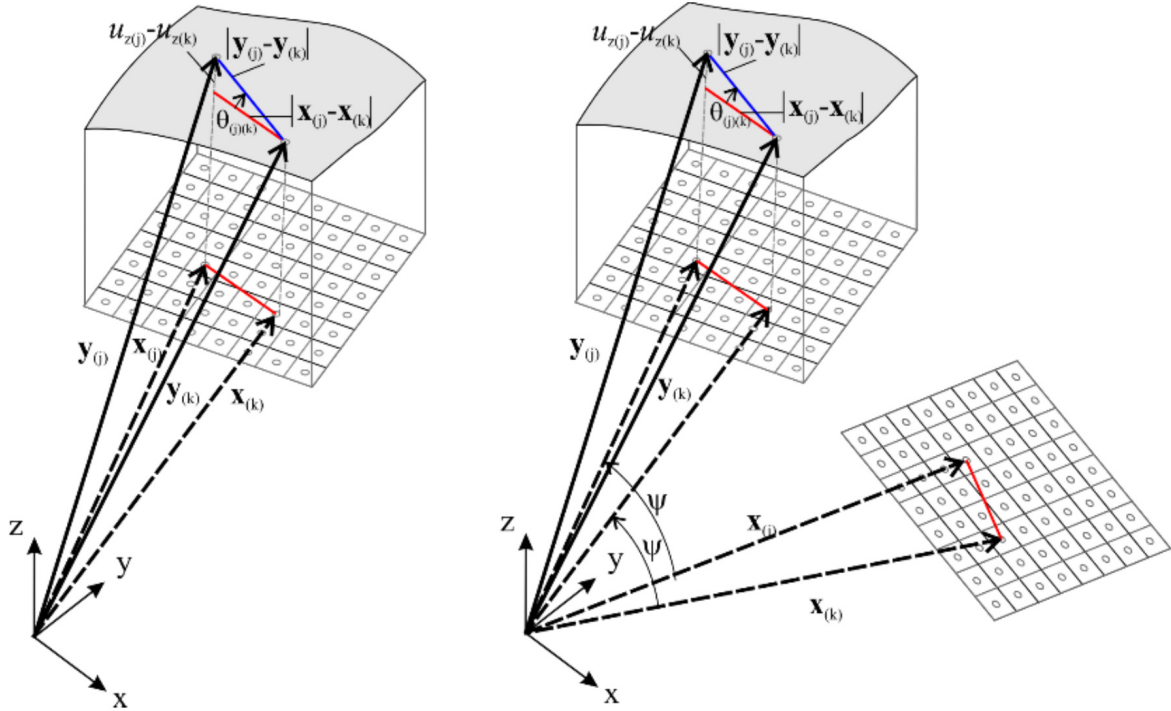


Figure 3. Kinematics of peridynamic material points on the cross-section: (left) anti-plane shear deformation, and (right) torsional deformation.

For torsional deformation, these material points experience the displacements $\mathbf{u}_{(j)}^T = \{-\psi z y_{(j)}, \psi z x_{(j)}, u_{z(j)}\}$ and $\mathbf{u}_{(k)}^T = \{-\psi z y_{(k)}, \psi z x_{(k)}, u_{z(k)}\}$, in which ψ represents the angle of twist. Their relative position can be expressed as

$$\mathbf{y}_{(j)} - \mathbf{y}_{(k)} = \mathbf{x}_{(j)} - \mathbf{x}_{(k)} + \Omega \times (\mathbf{x}_{(j)} - \mathbf{x}_{(k)}) + (u_{z(j)} - u_{z(k)})\mathbf{e}_z, \quad (3)$$

in which $\Omega^T = \{0, 0, \psi z\}$, and the product term $\Omega \times (\mathbf{x}_{(j)} - \mathbf{x}_{(k)})$ represents the rotation of $(\mathbf{x}_{(j)} - \mathbf{x}_{(k)})$ around the z -axis, resulting in no deformation.

As shown in Figure 3, the relative out-of-plane displacement (elevation) of material points $\mathbf{x}_{(j)}$ and $\mathbf{x}_{(k)}$ is defined as

$$e_{(k)(j)} = u_{z(j)} - u_{z(k)}. \quad (4)$$

Also, under small deformations, the slope of this elevation (change in angle) between material points $\mathbf{x}_{(k)}$ and $\mathbf{x}_{(j)}$ is defined as

$$r_{(k)(j)} = \frac{e_{(k)(j)}}{\xi_{(k)(j)}} = \frac{u_{z(j)} - u_{z(k)}}{\xi_{(k)(j)}} \quad (5)$$

where $\xi_{(k)(j)} = |\mathbf{x}_{(j)} - \mathbf{x}_{(k)}|$ represents the distance between these material points.

3. Ordinary state-based peridynamics

Due to the interaction between material points $\mathbf{x}_{(k)}$ and $\mathbf{x}_{(j)}$, a scalar-valued micropotential, $w_{(k)(j)}$, develops; it depends on the material properties, as well as the elevation, $e_{(k)(j)}$, between point $\mathbf{x}_{(k)}$ and all other material points in its family. Note that $w_{(j)(k)} \neq w_{(k)(j)}$ because $w_{(j)(k)}$ depends on the state of material points within the family of material point $\mathbf{x}_{(j)}$. These micropotentials can be expressed as

$$w_{(k)(j)} = w_{(k)(j)}(e_{(1^k)(k)}, e_{(2^k)(k)}, \dots) \quad \text{and} \quad w_{(j)(k)} = w_{(j)(k)}(e_{(1^j)(j)}, e_{(2^j)(j)}, \dots), \quad (6)$$

in which $e_{(j)(k)} = u_{z(j)} - u_{z(k)}$ represents elevation between material points $\mathbf{x}_{(k)}$ and $\mathbf{x}_{(j)}$. The change in elevation, $e_{(m^k)(k)}$, is measured between point $\mathbf{x}_{(k)}$ and the m -th material point that interacts with point $\mathbf{x}_{(k)}$. Similarly, $e_{(m^j)(j)}$ is measured between point $\mathbf{x}_{(j)}$ and the m -th material point that interacts with point $\mathbf{x}_{(j)}$, as shown in Figure 2. The strain energy density, $W_{(k)}$, of material point $\mathbf{x}_{(k)}$ can be expressed as a summation of all the micropotentials, $w_{(k)(j)}$, arising from the interaction of material point $\mathbf{x}_{(k)}$ and the other material points, $\mathbf{x}_{(j)}$, within its horizon in the form

$$W_{(k)} = \frac{1}{2} \sum_{j=1}^{\infty} \frac{1}{2} [w_{(k)(j)}(e_{(1^k)(k)}, e_{(2^k)(k)}, \dots) + w_{(j)(k)}(e_{(1^j)(j)}, e_{(2^j)(j)}, \dots)] V_{(j)}, \quad (7)$$

in which $w_{(k)(j)} = 0$ for $k = j$.

The PD equation of motion at material point $\mathbf{x}_{(k)}$ can be derived by applying the principle of virtual work, i.e.,

$$\delta \int_{t_0}^{t_1} (T - U) dt = 0, \quad (8)$$

where T and U represent the total kinetic and potential energies in the body. This principle is satisfied by solving for the Euler–Lagrange equation

$$\frac{d}{dt} \left(\frac{\partial L}{\partial \dot{u}_{z(k)}} \right) - \frac{\partial L}{\partial u_{z(k)}} = 0 \quad (9)$$

where the Lagrangian L is defined as $L = T - U$.

The total kinetic and potential energies in the body can be obtained by summation of kinetic and potential energies of all material points, respectively,

$$T = \sum_{i=1}^{\infty} \frac{1}{2} \rho_{(i)} \dot{u}_{z(i)} \dot{u}_{z(i)} V_{(i)} \quad \text{and} \quad U = \sum_{i=1}^{\infty} W_{(i)} V_{(i)} - \sum_{i=1}^{\infty} (b_{z(i)} u_{z(i)}) V_{(i)}. \quad (10a)$$

Substituting for the strain energy density, $W_{(i)}$, of material point $\mathbf{x}_{(i)}$ from (7), the potential energy can be rewritten as

$$U = \sum_{i=1}^{\infty} \left\{ \frac{1}{2} \sum_{j=1}^{\infty} \frac{1}{2} [w_{(i)(j)}(e_{(1^i)(i)}, e_{(2^i)(i)}, \dots) + w_{(j)(i)}(e_{(1^j)(j)}, e_{(2^j)(j)}, \dots)] V_{(j)} - (b_{z(i)} u_{z(i)}) \right\} V_{(i)}. \quad (11)$$

The Lagrangian can be written in an expanded form by showing only the terms associated with the material point $\mathbf{x}_{(k)}$ as

$$\begin{aligned}
L = & \cdots + \frac{1}{2} \rho_{(k)} \dot{u}_{z(k)} \dot{u}_{z(k)} V_{(k)} + \cdots \\
& \cdots - \frac{1}{2} \sum_{j=1}^{\infty} \left\{ \frac{1}{2} [w_{(k)(j)}(e_{(1^k)(k)}, e_{(2^k)(k)}, \dots) + w_{(j)(k)}(e_{(1^j)(j)}, e_{(2^j)(j)}, \dots)] V_{(j)} \right\} V_{(k)} \cdots \\
& \cdots - \frac{1}{2} \sum_{i=1}^{\infty} \left\{ \frac{1}{2} [w_{(i)(k)}(e_{(1^i)(i)}, e_{(2^i)(i)}, \dots) + w_{(k)(i)}(e_{(1^k)(k)}, e_{(2^k)(k)}, \dots)] V_{(i)} \right\} V_{(k)} \cdots \\
& \cdots + (b_{z(k)} u_{z(k)}) V_{(k)} \cdots
\end{aligned} \tag{12a}$$

or

$$\begin{aligned}
L = & \cdots + \frac{1}{2} \rho_{(k)} \dot{u}_{z(k)} \dot{u}_{z(k)} V_{(k)} + \cdots \\
& \cdots - \frac{1}{2} \sum_{j=1}^{\infty} \{w_{(k)(j)}(e_{(1^k)(k)}, e_{(2^k)(k)}, \dots) V_{(j)} V_{(k)}\} \cdots \\
& \cdots - \frac{1}{2} \sum_{j=1}^{\infty} \{w_{(j)(k)}(e_{(1^j)(j)}, e_{(2^j)(j)}, \dots) V_{(j)} V_{(k)}\} \cdots \\
& \cdots + (b_{z(k)} u_{z(k)}) V_{(k)} \cdots .
\end{aligned} \tag{12b}$$

Substituting from (12b) into (9) results in the Euler–Lagrange equation of the material point $\mathbf{x}_{(k)}$ as

$$\begin{aligned}
\rho_{(k)} \ddot{u}_{z(k)} V_{(k)} + \left(\sum_{j=1}^{\infty} \frac{1}{2} \left(\sum_{i=1}^{\infty} \frac{\partial w_{(k)(j)}}{\partial (u_{z(j)} - u_{z(k)})} V_{(i)} \right) \frac{\partial (u_{z(j)} - u_{z(k)})}{\partial u_{z(k)}} \right. \\
\left. + \sum_{j=1}^{\infty} \frac{1}{2} \left(\sum_{i=1}^{\infty} \frac{\partial w_{(j)(k)}}{\partial (u_{z(k)} - u_{z(j)})} V_{(i)} \right) \frac{\partial (u_{z(k)} - u_{z(j)})}{\partial u_{z(k)}} - b_{z(k)} \right) V_{(k)} = 0 \tag{13a}
\end{aligned}$$

or

$$\rho_{(k)} \ddot{u}_{z(k)} = \sum_{j=1}^{\infty} \frac{1}{2} \left(\sum_{i=1}^{\infty} \frac{\partial w_{(k)(j)}}{\partial (u_{z(j)} - u_{z(k)})} V_{(i)} \right) - \sum_{j=1}^{\infty} \frac{1}{2} \left(\sum_{i=1}^{\infty} \frac{\partial w_{(j)(k)}}{\partial (u_{z(k)} - u_{z(j)})} V_{(i)} \right) + b_{z(k)} = 0, \tag{13b}$$

in which it is assumed that the interactions not involving material point $\mathbf{x}_{(k)}$ do not have any effect on material point $\mathbf{x}_{(k)}$. Based on the dimensional analysis of this equation, it is apparent that the quantity $\sum_{i=1}^{\infty} V_{(i)} \partial w_{(k)(i)} / \partial (u_{z(j)} - u_{z(k)})$ represents the force density in the z -direction that material point $\mathbf{x}_{(j)}$ exerts on material point $\mathbf{x}_{(k)}$ and the quantity $\sum_{i=1}^{\infty} V_{(i)} \partial w_{(i)(k)} / \partial (u_{z(k)} - u_{z(j)})$ represents the force density in the z -direction that material point $\mathbf{x}_{(k)}$ exerts on material point $\mathbf{x}_{(j)}$. With this interpretation, (13b) can be rewritten as

$$t_{z(k)(j)}(e_{(j)(k)}, \mathbf{x}_{(j)} - \mathbf{x}_{(k)}, t) = \frac{1}{2} \frac{1}{V_{(j)}} \sum_{i=1}^{\infty} \frac{\partial w_{(k)(i)}}{\partial (u_{z(j)} - u_{z(k)})} V_{(i)}, \tag{14a}$$

and

$$t_{z(j)(k)}(e_{(k)(j)}, \mathbf{x}_{(k)} - \mathbf{x}_{(j)}, t) = \frac{1}{2} \frac{1}{V_{(j)}} \sum_{i=1}^{\infty} \frac{\partial w_{(i)(k)}}{\partial (u_{z(k)} - u_{z(j)})} V_{(i)}, \tag{14b}$$

in which $V_{(j)}$ represents the volume of material point $\mathbf{x}_{(j)}$. The material point $\mathbf{x}_{(j)}$ exerts the force density $t_{z(k)(j)}$ on material point $\mathbf{x}_{(k)}$.

By utilizing the state concept described by Silling et al. [2007] and Silling and Lehoucq [2010], the force densities $t_{z(k)(j)}$ and $t_{z(j)(k)}$ can be stored in force scalar states that belong to material points $\mathbf{x}_{(k)}$ and $\mathbf{x}_{(j)}$, respectively, as

$$\underline{t}_z(\mathbf{x}_{(k)}, t) = \begin{Bmatrix} \vdots \\ t_{z(k)(j)} \\ \vdots \end{Bmatrix} \quad \text{and} \quad \underline{t}_z(\mathbf{x}_{(j)}, t) = \begin{Bmatrix} \vdots \\ t_{z(j)(k)} \\ \vdots \end{Bmatrix}. \quad (15)$$

The force densities $t_{z(k)(j)}$ and $t_{z(j)(k)}$ stored in scalar states $\underline{t}_z(\mathbf{x}_{(k)}, t)$ and $\underline{t}_z(\mathbf{x}_{(j)}, t)$ can be extracted again by operating the force states on the corresponding initial relative position vectors, $(\mathbf{x}_{(j)} - \mathbf{x}_{(k)})$ and $(\mathbf{x}_{(k)} - \mathbf{x}_{(j)})$, as

$$t_{z(k)(j)} = \underline{t}_z(\mathbf{x}_{(k)}, t) \langle \mathbf{x}_{(j)} - \mathbf{x}_{(k)} \rangle \quad \text{and} \quad t_{z(j)(k)} = \underline{t}_z(\mathbf{x}_{(j)}, t) \langle \mathbf{x}_{(k)} - \mathbf{x}_{(j)} \rangle. \quad (16)$$

By using (14a)–(14b), the Euler–Lagrange equation of the material point $\mathbf{x}_{(k)}$ can be recast as

$$\rho_{(k)} \ddot{u}_{z(k)} = \sum_{j=1}^{\infty} [t_{z(k)(j)}(e_{(j)(k)}, \mathbf{x}_{(j)} - \mathbf{x}_{(k)}, t) - t_{z(j)(k)}(e_{(k)(j)}, \mathbf{x}_{(k)} - \mathbf{x}_{(j)}, t)] V_{(j)} + b_{z(k)}. \quad (17)$$

Because the area of each material point $V_{(j)}$ is infinitesimally small, for the limiting case of $V_{(j)} \rightarrow 0$, the infinite summation can be expressed as a Riemann integral while considering only the material points within the horizon. Therefore, (17) can be rewritten in integral equation form as

$$\rho \ddot{u}_z = \int_H [t_z(u'_{(z)} - u_{(z)}, \mathbf{x}' - \mathbf{x}, t) - t'_z(u_{(z)} - u'_{(z)}, \mathbf{x} - \mathbf{x}', t)] dV_{x'} + b_z \quad (18)$$

in which $u_{(z)}$ and $u'_{(z)}$ represent the transverse displacement at material points \mathbf{x} and \mathbf{x}' , respectively. Depending on the boundary conditions, the solution to this equation provides either the antiplane or torsional deformation.

3.1. Peridynamic force density. The force densities at material points $\mathbf{x}_{(k)}$ and $\mathbf{x}_{(j)}$ can be defined in the form

$$t_{z(k)(j)}(e_{(j)(k)}, \mathbf{x}_{(j)} - \mathbf{x}_{(k)}, t) = \frac{1}{2} A_{(k)(j)} \quad \text{and} \quad t_{z(j)(k)}(e_{(k)(j)}, \mathbf{x}_{(k)} - \mathbf{x}_{(j)}, t) = -\frac{1}{2} B_{(k)(j)}, \quad (19)$$

where $A_{(k)(j)}$ and $B_{(k)(j)}$ are auxiliary parameters that are dependent on engineering material constants, the deformation field, and the horizon.

In light of the definition (14) of the expressions for force density in terms of micropotentials, the force density vectors can be related to the strain energy density function, $W_{(k)}$, at material point $\mathbf{x}_{(k)}$ as

$$t_{z(k)(j)}(u_{z(j)} - u_{z(k)}, \mathbf{x}_{(j)} - \mathbf{x}_{(k)}, t) = \frac{1}{V_{(j)}} \frac{\partial W_{(k)}}{\partial (u_{z(j)} - u_{z(k)})}, \quad (20a)$$

$$t_{z(j)(k)}(u_{z(k)} - u_{z(j)}, \mathbf{x}_{(k)} - \mathbf{x}_{(j)}, t) = \frac{1}{V_{(k)}} \frac{\partial W_{(j)}}{\partial (u_{z(k)} - u_{z(j)})}. \quad (20b)$$

However, the determination of the auxiliary parameters, $A_{(k)(j)}$ and $B_{(k)(j)}$, requires an explicit form of the strain energy density function.

3.2. Peridynamic material parameters. For an isotropic and elastic material experiencing antiplane and torsional deformation, the classical expression for the strain energy density, $W_{(k)}$, at material point $\mathbf{x}_{(k)}$ can be written as

$$W_{(k)} = \frac{1}{2}\mu[\gamma_{(k)xz}^2 + \gamma_{(k)yz}^2] \quad (21)$$

in which μ is the shear modulus of the material, and $\gamma_{(k)xz}$ and $\gamma_{(k)yz}$ are the transverse shear strain components at material point $\mathbf{x}_{(k)}$.

Analogous to (21), the PD representation of the strain energy density, $W_{(k)}$, at material point $\mathbf{x}_{(k)}$ can be expressed as

$$W_{(k)} = a[r_{(k)xz}^2 + r_{(k)yz}^2], \quad (22)$$

in which a is the ordinary state-based PD material parameter for strain energy and $r_{(k)xz}$ and $r_{(k)yz}$ are defined in the form

$$r_{(k)xz} = b \sum_{j=1}^N w_{(k)(j)} e_{(j)(k)} \cos \theta_{(k)(j)} V_{(j)} \quad \text{and} \quad r_{(k)yz} = b \sum_{j=1}^N w_{(k)(j)} e_{(j)(k)} \sin \theta_{(k)(j)} V_{(j)}, \quad (23)$$

in which $\cos \theta_{(k)(j)} = (x_{(j)} - x_{(k)})/\xi_{(k)(j)}$ and $\sin \theta_{(k)(j)} = (y_{(j)} - y_{(k)})/\xi_{(k)(j)}$, N represents the number of material points within the family of $\mathbf{x}_{(k)}$, and b is a PD parameter. The nondimensional influence function, which can be taken in the form of $w_{(k)(j)} = \delta/\xi_{(k)(j)}$, provides a means to control the influence of material points away from the current material point at $\mathbf{x}_{(k)}$. The infinitesimal volume of the material point $\mathbf{x}_{(j)}$ is denoted by $V_{(j)} = \ell \xi_{(k)(j)} \Delta \xi_{(k)(j)} \Delta \theta_{(k)(j)}$, where $\Delta \xi_{(k)(j)}$ and $\Delta \theta_{(k)(j)}$ represent the incremental distance and angle between material points $\mathbf{x}_{(k)}$ and $\mathbf{x}_{(j)}$ and ℓ is the length of the component.

As the horizon approaches zero, the out-of-plane displacement at material point $\mathbf{x}_{(j)}$ can be expressed by using a Taylor series expansion as

$$u_{z(j)} - u_{z(k)} = u_{z(k),x} \xi_{(k)(j)} \cos \theta_{(k)(j)} + u_{z(k),y} \xi_{(k)(j)} \sin \theta_{(k)(j)} + \frac{1}{2} u_{z(k),xx} \xi_{(k)(j)}^2 \cos^2 \theta_{(k)(j)} \\ + u_{z(k),xy} \xi_{(k)(j)}^2 \cos \theta_{(k)(j)} \sin \theta_{(k)(j)} + \frac{1}{2} u_{z(k),yy} \xi_{(k)(j)}^2 \sin^2 \theta_{(k)(j)}. \quad (24)$$

Substituting from (24) into (23) along with the infinitesimal volume and influence function, performing algebraic manipulations, and converting the summations to integrations lead to

$$r_{(k)xz} = b \frac{\ell \pi \delta^3}{2} u_{z(k),x} \quad \text{and} \quad r_{(k)yz} = b \frac{\ell \pi \delta^3}{2} u_{z(k),y}. \quad (25)$$

Defining $b = 2/(\ell \pi \delta^3)$ reduces $r_{(k)xz}$ and $r_{(k)yz}$ to the classical transverse shear strains $\gamma_{(k)xz}$ and $\gamma_{(k)yz}$; thus, equating the peridynamic and classical strain energy density, $W_{(k)}$, at material point $\mathbf{x}_{(k)}$ results in

$$W_{(k)} = a[r_{(k)xz}^2 + r_{(k)yz}^2] = \frac{1}{2}\mu[\gamma_{(k)xz}^2 + \gamma_{(k)yz}^2]. \quad (26)$$

It yields the ordinary state-based peridynamic material parameter for strain energy as

$$a = \frac{1}{2}\mu, \quad (27)$$

which is not dependent on the horizon, unlike the parameter b . The parameters, $r_{(k)xz}$ and $r_{(k)yz}$, can be viewed as the peridynamic transverse shear angles.

3.3. Force density-displacement relation. Substituting for $W_{(k)}$ in (20) and differentiating, the force density, $t_{z(k)(j)}$, can be obtained as

$$t_{z(k)(j)}(u_{z(j)} - u_{z(k)}, \mathbf{x}_{(j)} - \mathbf{x}_{(k)}, t) = \mu \left[w_{(k)(j)} \frac{x_{(j)} - x_{(k)}}{\xi_{(k)(j)}} r_{(k)xz} + w_{(k)(j)} \frac{y_{(j)} - y_{(k)}}{\xi_{(k)(j)}} r_{(k)yz} \right], \quad (28a)$$

$$t_{z(j)(k)}(u_{z(k)} - u_{z(j)}, \mathbf{x}_{(k)} - \mathbf{x}_{(j)}, t) = \mu \left[w_{(j)(k)} \frac{x_{(k)} - x_{(j)}}{\xi_{(k)(j)}} r_{(j)xz} + w_{(j)(k)} \frac{y_{(k)} - y_{(j)}}{\xi_{(k)(j)}} r_{(j)yz} \right]. \quad (28b)$$

Comparison of (28) and (19) leads to the determination of $A_{(k)(j)}$ and $B_{(k)(j)}$ as

$$A_{(k)(j)} = 2\mu \left[w_{(k)(j)} \frac{x_{(j)} - x_{(k)}}{\xi_{(k)(j)}} r_{(k)xz} + w_{(k)(j)} \frac{y_{(j)} - y_{(k)}}{\xi_{(k)(j)}} r_{(k)yz} \right], \quad (29a)$$

$$B_{(j)(k)} = 2\mu \left[w_{(j)(k)} \frac{x_{(j)} - x_{(k)}}{\xi_{(k)(j)}^2} r_{(j)xz} + w_{(j)(k)} \frac{y_{(j)} - y_{(k)}}{\xi_{(k)(j)}^2} r_{(j)yz} \right]. \quad (29b)$$

After substituting for the force densities, the final form of the equation of motion becomes

$$\rho_{(k)} \ddot{u}_{z(k)} = \mu \sum_{j=1}^{\infty} w_{(k)(j)} \left[(r_{(k)xz} + r_{(j)xz}) \frac{x_{(j)} - x_{(k)}}{\xi_{(k)(j)}} + (r_{(k)yz} + r_{(j)yz}) \frac{y_{(j)} - y_{(k)}}{\xi_{(k)(j)}} \right] V_{(j)} + b_{z(k)}, \quad (30a)$$

with

$$r_{(k)xz} = \frac{2}{\ell\pi\delta^3} \sum_{j=1}^N w_{(k)(j)} e_{(j)(k)} \cos \theta_{(k)(j)} V_{(j)}, \quad (30b)$$

$$r_{(k)yz} = \frac{2}{\ell\pi\delta^3} \sum_{j=1}^N w_{(k)(j)} e_{(j)(k)} \sin \theta_{(k)(j)} V_{(j)}. \quad (30c)$$

4. Bond-based peridynamics

In the case of pairwise interaction only between material points $\mathbf{x}_{(i)}$ and $\mathbf{x}_{(j)}$, the micropotential, $w_{(i)(j)}$, is a function of $e_{(i)(j)}$. Thus, the total potential energy can be obtained by the summation of the micropotentials $w_{(i)(j)}(e_{(i)(j)})$ arising from deformation only between two material points within the same family

$$U = \sum_{i=1}^{\infty} \left\{ \frac{1}{2} \sum_{j=1}^{\infty} \frac{1}{2} [w_{(i)(j)}(e_{(i)(j)}) + w_{(j)(i)}(e_{(j)(i)})] V_{(j)} - (b_{z(i)} u_{z(i)}) \right\} V_{(i)}. \quad (31)$$

For a pairwise interaction, the Euler–Lagrange equation results in

$$\begin{aligned} \rho_{(k)} \ddot{u}_{z(k)} V_{(k)} + \left(\sum_{j=1}^{\infty} \frac{1}{2} \left(\frac{\partial w_{(k)(j)}}{\partial (u_{z(j)} - u_{z(k)})} \right) \frac{\partial (u_{z(j)} - u_{z(k)})}{\partial u_{z(k)}} \right. \\ \left. + \sum_{j=1}^{\infty} \frac{1}{2} \left(\frac{\partial w_{(j)(k)}}{\partial (u_{z(k)} - u_{z(j)})} \right) \frac{\partial (u_{z(k)} - u_{z(j)})}{\partial u_{z(k)}} - b_{z(k)} \right) V_{(k)} = 0. \quad (32) \end{aligned}$$

This equation can be rewritten as

$$\rho^{(k)}\ddot{u}_{z(k)} + \sum_{j=1}^{\infty} \frac{1}{2} [-f_{z(k)(j)} + f_{z(j)(k)}] V_{(j)} - b_{z(k)} = 0, \quad (33)$$

in which $f_{z(k)(j)}$ and $f_{z(j)(k)}$ are defined as

$$f_{z(k)(j)} = \frac{\partial w_{(k)(j)}}{\partial (u_{z(j)} - u_{z(k)})} \quad \text{and} \quad f_{z(j)(k)} = \frac{\partial w_{(j)(k)}}{\partial (u_{z(k)} - u_{z(j)})}. \quad (34)$$

They represent the PD interaction forces between the material points $\mathbf{x}_{(k)}$ and $\mathbf{x}_{(j)}$ arising from the deformation (elevation). For a linear material behavior, they can be defined in the form

$$f_{z(k)(j)} = cr_{(k)(j)} \quad \text{and} \quad f_{z(j)(k)} = cr_{(j)(k)} \quad (35)$$

or

$$f_{z(k)(j)} = cr_{(k)(j)} \quad \text{and} \quad f_{z(j)(k)} = -cr_{(k)(j)}. \quad (36)$$

With these definitions, the equation of motion, Equation (33), becomes

$$\rho\ddot{u}_{z(k)} = c \sum_{j=1}^{\infty} r_{(k)(j)} V_{(j)} + b_{z(k)} \quad (37a)$$

or

$$\rho\ddot{u}_{z(k)} = c \sum_{j=1}^{\infty} \frac{u_{z(j)} - u_{z(k)}}{\xi_{(k)(j)}} V_{(j)} + b_{z(k)}, \quad (37b)$$

in which c is the PD material parameter (bond constant) associated with the antiplane and torsional deformations.

As the horizon approaches zero, (37) must recover its classical counterpart, given as

$$\rho\ddot{u}_z = \mu(u_{z,xx} + u_{z,yy}). \quad (38)$$

Representing the out-of-plane displacement at material point $\mathbf{x}_{(j)}$ by using a Taylor series expansion as in (24), substituting it into (37) along with the infinitesimal volume, and performing algebraic manipulations after converting the summations to integrations lead to

$$\rho\ddot{u}_{z(k)} = c \frac{\pi \ell \delta^3}{6} (u_{z(k),xx} + u_{z(k),yy}). \quad (39)$$

Comparison of the bond-based PD equation of motion with its classical counterpart leads to the determination of the PD bond constant, c , as

$$c = \frac{6\mu}{\pi \ell \delta^3}, \quad (40)$$

which is dependent on the horizon. The final form of the bond-based PD equation of motion becomes

$$\rho\ddot{u}_{z(k)} = \frac{6\mu}{\pi \ell \delta^3} \sum_{j=1}^{\infty} \frac{u_{z(j)} - u_{z(k)}}{\xi_{(k)(j)}} V_{(j)}. \quad (41)$$

Alternatively, in light of (34) and (35), the bond constant can also be determined by considering the explicit expression for the micropotentials in the form

$$w_{(k)(j)} = \frac{1}{2}c\xi_{(k)(j)}r_{(k)(j)}^2 \quad \text{and} \quad w_{(j)(k)} = \frac{1}{2}c\xi_{(k)(j)}r_{(j)(k)}^2. \quad (42)$$

Therefore, the strain energy density at material point $\mathbf{x}_{(k)}$ can be obtained from (7) as

$$W_{(k)} = c \frac{1}{2} \sum_{j=1}^{\infty} \frac{1}{2} \xi_{(k)(j)} r_{(k)(j)}^2 V_{(j)}. \quad (43)$$

Substituting for the slope and infinitesimal volume and converting the summation to integration lead to

$$W_{(k)} = \ell c \frac{1}{2} \int_0^{\delta} \int_0^{2\pi} \frac{1}{2} (u_{z(j)} - u_{z(k)})^2 d\xi d\theta. \quad (44)$$

The peridynamic bond constant, c , can be determined by equating the strain energies from classical continuum mechanics and peridynamics for a specified simple deformation such as $w(x, y) = (x + y)$. For the material point of interest located at $(x_{(k)} = 0, y_{(k)} = 0)$, the elevation is $e_{(k)(j)} = (x' + y')$ and $\xi = \xi_{(k)(j)} = \sqrt{x'^2 + y'^2}$. Thus, the peridynamic strain energy density can be obtained as

$$W_{(k)} = \ell c \frac{1}{2} \int_0^{\delta} \int_0^{2\pi} \frac{1}{2} (u_{z(j)} - u_{z(k)})^2 d\xi d\theta = \ell c \frac{1}{2} \int_0^{\delta} \int_0^{2\pi} \frac{1}{2} \xi^2 d\xi d\theta = \frac{\ell c \pi \delta^3}{6}. \quad (45)$$

The corresponding strain energy density based on classical continuum mechanics can be written as

$$W = \frac{1}{2}(\sigma_{xz}\gamma_{xz} + \sigma_{yz}\gamma_{yz}) = \frac{1}{2}\mu(u_{z,x}^2 + u_{z,y}^2) = \mu. \quad (46)$$

Equating the strain energies from peridynamics and the classical continuum mechanics leads to the determination of the PD material parameter, $c = 6\mu/\pi\ell\delta^3$, which is the same as in (40).

5. Correction of PD material parameters

The PD material parameters b and c are determined for material points with a horizon completely embedded in the material. The values of these parameters depend on the domain of integration defined by the horizon. Therefore, their values require correction if the material point is close to free surfaces or material interfaces (Figure 4). Since the presence of free surfaces is problem-dependent, it is impractical to resolve this issue analytically.

5.1. Surface correction. The bond-based and ordinary state-based PD parameters are corrected by comparing the PD and classical expressions for the strain energy density and shear strain components for two different simple loading conditions. The correction for the parameter c is achieved by comparing the strain energy densities, and for the parameter b by comparing the shear strain components.

The first loading case is a simple linear displacement distribution in the x -direction given by

$$u_z = \zeta x. \quad (47)$$

The second loading case is a simple linear displacement distribution in the y -direction given by

$$u_z = \zeta y. \quad (48)$$

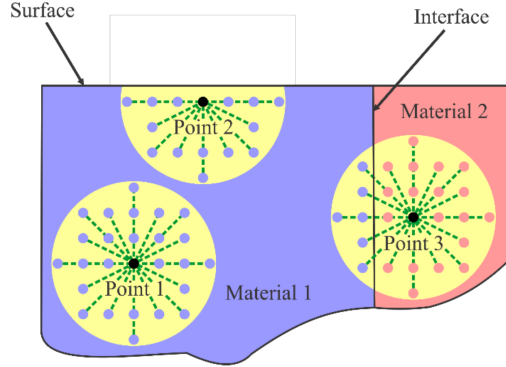


Figure 4. Surface effects in the domain of interest.

Due to these loading conditions, the corresponding PD strain energy density and shear strain can be obtained from (43) and (23) as

$$W_{(k)x}^{\text{PD}} = \zeta^2 c \frac{1}{2} \sum_{j=1}^N \frac{1}{2} \frac{1}{\xi_{(k)(j)}} (x_{(j)} - x_{(k)})^2 V_{(j)}, \quad W_{(k)y}^{\text{PD}} = \zeta^2 c \frac{1}{2} \sum_{j=1}^N \frac{1}{2} \frac{1}{\xi_{(k)(j)}} (y_{(j)} - y_{(k)})^2 V_{(j)} \quad (49)$$

and

$$r_{(k)xz} = \zeta b \sum_{j=1}^N w_{(k)(j)} (x_{(j)} - x_{(k)}) \cos \theta_{(k)(j)} V_{(j)}, \quad r_{(k)yz} = b \zeta \sum_{j=1}^N w_{(k)(j)} (y_{(j)} - y_{(k)}) \sin \theta_{(k)(j)} V_{(j)}, \quad (50)$$

with N representing the number of material points inside the horizon of $\mathbf{x}_{(k)}$. For these loading conditions, the classical strain energy of a material point $W_{(k)}^{\text{CCM}}$ and shear strain components are

$$W_{(k)x}^{\text{CCM}} = \frac{1}{2} \mu \zeta^2 \quad \text{and} \quad W_{(k)y}^{\text{CCM}} = \frac{1}{2} \mu \zeta^2 \quad (51)$$

and

$$\gamma_{(k)xz} = \zeta \quad \text{and} \quad \gamma_{(k)yz} = \zeta. \quad (52)$$

The correction factors for these loading conditions at material point $\mathbf{x}_{(k)}$ can be determined as

$$g_{x(k)} = \frac{W_{(k)x}^{\text{CCM}}}{W_{(k)x}^{\text{PD}}} \quad \text{and} \quad g_{(k)xz} = \frac{\gamma_{(k)xz}}{r_{(k)xz}} \quad (53)$$

and

$$g_{y(k)} = \frac{W_{(k)y}^{\text{CCM}}}{W_{(k)y}^{\text{PD}}} \quad \text{and} \quad g_{(k)yz} = \frac{\gamma_{(k)yz}}{r_{(k)yz}}. \quad (54)$$

With these correction factors, the final form of the ordinary state-based PD equation become

$$\rho(k) \ddot{u}_z(k) = \mu \sum_{j=1}^{\infty} w_{(k)(j)} \left[(r_{(k)xz} g_{(k)xz} + r_{(j)xz} g_{(j)xz}) \frac{x_{(j)} - x_{(k)}}{\xi_{(k)(j)}} + (r_{(k)yz} g_{(k)yz} + r_{(j)yz} g_{(j)yz}) \frac{y_{(j)} - y_{(k)}}{\xi_{(k)(j)}} \right] V_{(j)} + b_z(k), \quad (55)$$

in which

$$r_{(k)xz} = b \sum_{j=1}^N w_{(k)(j)} e_{(j)(k)} g_{(k)xz} \cos \theta_{(k)(j)} V_{(j)}, \quad r_{(k)yz} = b \sum_{j=1}^N w_{(k)(j)} e_{(j)(k)} g_{(k)yz} \sin \theta_{(k)(j)} V_{(j)}. \quad (56)$$

For the bond-based parameter, the correction factors can be obtained by taking their mean value as

$$\bar{g}_{(k)(j)x} = \frac{g_{x(k)} + g_{x(j)}}{2} \quad \text{and} \quad \bar{g}_{(k)(j)y} = \frac{g_{y(k)} + g_{y(j)}}{2}, \quad (57)$$

which may represent the principal axis of an ellipsoid. As introduced by Kilic [2008], the correction factor between arbitrary material points $\mathbf{x}_{(k)}$ and $\mathbf{x}_{(j)}$ can be calculated by

$$G_{(k)(j)} = [(n_x / \bar{g}_{(k)(j)x})^2 + (n_y / \bar{g}_{(k)(j)y})^2]^{-1/2}, \quad (58)$$

where n_x and n_y are direction cosines of $\mathbf{n} = (\mathbf{x}_{(j)} - \mathbf{x}_{(k)}) / |\mathbf{x}_{(j)} - \mathbf{x}_{(k)}|$. The final form of the bond-based PD equation including the correction factor for material point $\mathbf{x}_{(k)}$ becomes

$$\rho \ddot{u}_{z(k)} = \frac{6\mu}{\pi \ell \delta^3} \sum_{j=1}^{\infty} G_{(k)(j)} \frac{u_{z(j)} - u_{z(k)}}{\xi_{(k)(j)}} V_{(j)}. \quad (59)$$

5.2. Dissimilar material interface. The correction at the interface is achieved by using equivalent PD material parameters [Oterkus et al. 2014]. As shown in Figure 5, the material point $\mathbf{x}_{(i)}$ may interact with material points $\mathbf{x}_{(j)}$ and $\mathbf{x}_{(m)}$. Material points $\mathbf{x}_{(i)}$ and $\mathbf{x}_{(j)}$ are embedded in material 1, and $\mathbf{x}_{(m)}$ is embedded in material 2. The PD material parameter between points $\mathbf{x}_{(i)}$ and $\mathbf{x}_{(j)}$ is $a_{(i)(j)}$, and it differs from $a_{(i)(m)}$ between material points $\mathbf{x}_{(i)}$ and $\mathbf{x}_{(m)}$. Because the material points $\mathbf{x}_{(i)}$ and $\mathbf{x}_{(m)}$ are embedded in two different materials, their material parameter, $a_{(i)(m)}$, can be expressed in terms of an equivalent material constant as

$$a_{(i)(m)} = \frac{\ell_1 + \ell_2}{\ell_1/a_1 + \ell_2/a_2}, \quad (60)$$

in which ℓ_1 represents the segment of the distance between material points $\mathbf{x}_{(i)}$ and $\mathbf{x}_{(m)}$ in material 1, whose material parameter is a_1 , and ℓ_2 represents the segment in material 2, whose material parameter is a_2 .

6. Boundary conditions

Unlike the local theory, the PD boundary conditions are imposed through a nonzero volume of fictitious boundary layers. This necessity arises because the PD field equations do not contain any spatial derivatives; therefore, constraint conditions are, in general, not necessary for the solution of an integro-differential equation of motion. However, such conditions can be imposed by prescribing constraints on the displacement or transverse shear stress components in a fictitious boundary layer.

6.1. Displacement constraints. This type of boundary condition can be achieved through a fictitious region, \mathcal{R}_f . Therefore, a fictitious boundary layer with depth δ is introduced along the boundary of the actual material region, \mathcal{R} , as shown in Figure 6. Based on numerical experiments, Macek and Silling

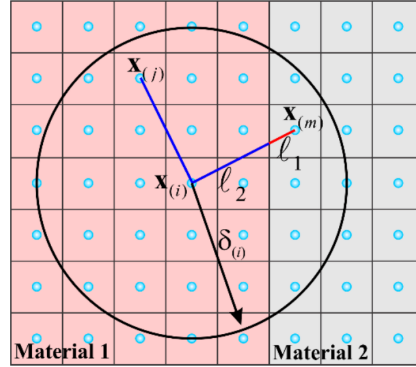


Figure 5. Interaction of material points across the interface.

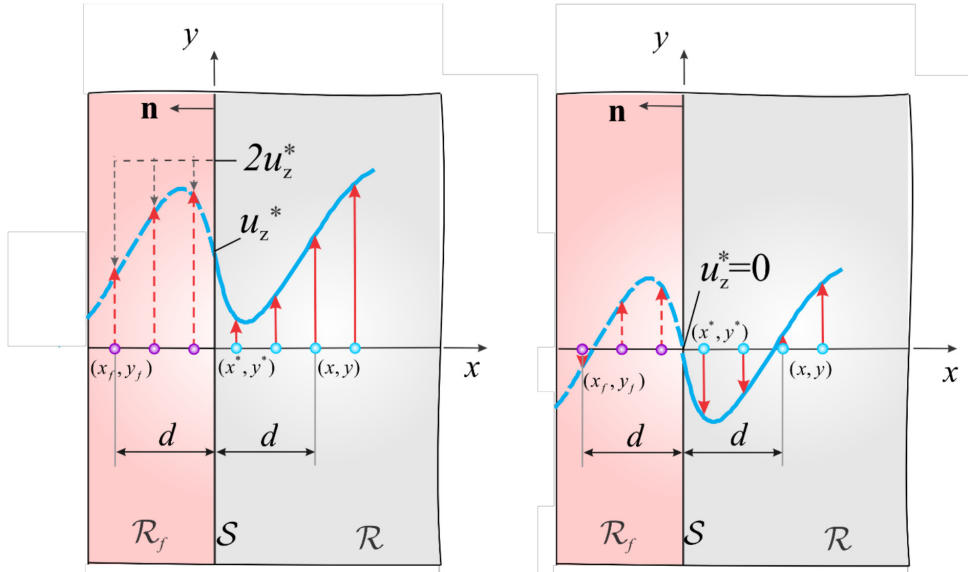


Figure 6. Imposing displacement constraints on the boundary: (left) nonzero constraint $u_z(x^*, y^*, t) = u_z^*$, and (right) zero constraint $u_z(x^*, y^*, t) = u_z^* = 0$.

[2007] suggest that the extent of the fictitious boundary layer be equal to the horizon, δ , in order to ensure that the imposed prescribed constraints are accurately reflected in the real domain.

The prescribed boundary value, $u_z^*(x^*, y^*, t)$, is imposed through a layer of the fictitious region, \mathcal{R}_f , along the boundary of the material surface, \mathcal{S} , as

$$u_z(x_f, y_f, t + \Delta t) = 2u_z^*(x^*, y^*, t + \Delta t) - u_z(x, y, t) \tag{61a}$$

with

$$(x^*, y^*) \in \mathcal{S}, \quad (x_f, y_f) \in \mathcal{R}_f, \quad (x, y) \in \mathcal{R}, \tag{61b}$$

in which (x, y) represents the position of a material point in \mathcal{R} , and (x^*, y^*) represents the location of a point on the boundary surface, \mathcal{S} . The location of the image material point in \mathcal{R}_f is denoted by (x_f, y_f) . The implementation of the prescribed boundary value of the displacement is depicted in Figure 6. In the case of $u_z^*(x^*, y^*, t) = 0$, this condition becomes

$$u_z(x_f, y_f, t + \Delta t) = -u_z(x, y, t). \quad (62)$$

6.2. Conditions on transverse shear stress components. Similar to the displacement boundary conditions, the transverse shear stress conditions are imposed through a fictitious region, \mathcal{R}_f . In the case of antiplane shear deformation, applied transverse shear stress on the boundary, $\sigma_{\alpha z}(x^*, y^*, t) = \tau_\alpha$ with $\alpha = x, y$, is imposed as (Figure 7, left)

$$\sigma_{\alpha z}(x^*, y^*, t) = \mu \left[\frac{\partial u_z}{\partial \alpha}(x^*, y^*) \right] = \tau_\alpha \quad (63a)$$

or

$$\frac{\partial u_z}{\partial \alpha}(x^*, y^*) = \frac{\tau_\alpha}{\mu}, \quad (63b)$$

which can be enforced as

$$u_z(x_f, y_f) = \frac{1}{\mu} \tau_\alpha (\alpha_f - \alpha) + u_z(x, y). \quad (63c)$$

For a zero transverse shear stress condition, i.e., $\sigma_{\alpha z}(x^*, y^*, t) = 0$, this expression reduces to

$$u_z(x^*, y^*) = u_z(x, y). \quad (64)$$

In the case of torsional deformation, zero shear stress boundary conditions are imposed as

$$\sigma_{xz}(x^*, y^*, t) = \mu \left[\frac{\partial u_z}{\partial x}(x^*, y^*) - \psi(y - y_0) \right] = 0, \quad (65a)$$

$$\sigma_{yz}(x^*, y^*, t) = \mu \left[\frac{\partial u_z}{\partial y}(x^*, y^*) - \psi(x - x_0) \right] = 0 \quad (65b)$$

or

$$\frac{\partial u_z}{\partial x}(x^*, y^*) = \frac{1}{\mu} \psi(y - y_0), \quad (66a)$$

$$\frac{\partial u_z}{\partial y}(x^*, y^*) = \frac{1}{\mu} \psi(x - x_0), \quad (66b)$$

which can be imposed as

$$u_z(x_f, y_f) = \frac{1}{\mu} \psi(y - y_0)(x_f - x) + u_z(x, y), \quad (67a)$$

$$u_z(x_f, y_f) = \frac{1}{\mu} \psi(x - x_0)(y_f - y) + u_z(x, y), \quad (67b)$$

in which ψ represents the applied angle of twist and (x_0, y_0) denote the coordinates of the reference point.

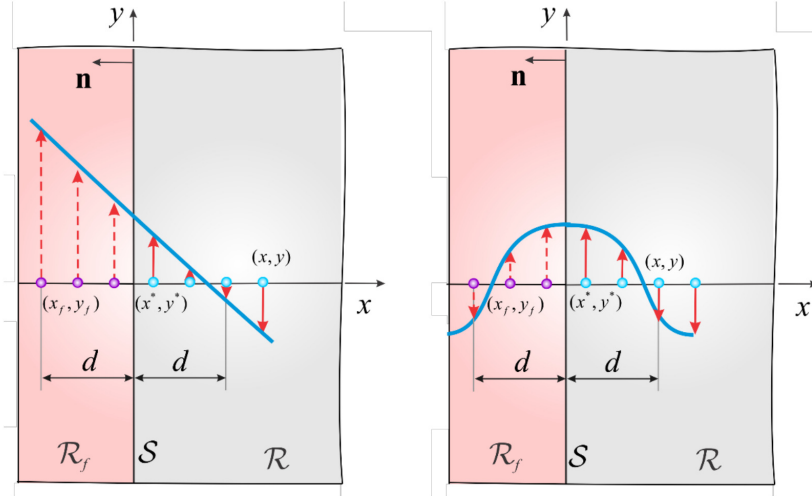


Figure 7. Material points and their image in the fictitious region for imposing (left) nonzero flux, and (right) zero flux.

7. Failure prediction

Damage is introduced through elimination of interactions (micropotentials) among the material points. It is assumed that when the change in angle (transverse shear strain), $r_{(k)(j)}$, between two material points, k and j , exceeds its critical value, r_c , the onset of damage occurs. Damage is reflected in the equations of motion by removing the force density vectors between the material points in an irreversible manner. Therefore, the force density vectors $t_{z(k)(j)}$ and $t_{z(j)(k)}$ in the case of the ordinary state-based form of the equations of motion and $f_{z(k)(j)}$ and $f_{z(j)(k)}$ in the case of the bond-based form can be modified through a history-dependent scalar-valued function $H(t, x_{(j)} - x_{(k)})$ [Silling and Askari 2005] as

$$t_{z(k)(j)} = H(t, x_{(j)} - x_{(k)})t_{z(k)(j)} \quad \text{and} \quad t_{z(j)(k)} = H(t, x_{(k)} - x_{(j)})t_{z(j)(k)} \quad (68)$$

and

$$f_{z(k)(j)} = H(t, x_{(j)} - x_{(k)})f_{z(k)(j)} \quad \text{and} \quad f_{z(j)(k)} = H(t, x_{(k)} - x_{(j)})f_{z(j)(k)} \quad (69)$$

in which a history-dependent scalar-valued function H is defined as

$$H(t, x_{(j)} - x_{(k)}) = \begin{cases} 1 & \text{if } r_{(k)(j)}(t', x_{(j)} - x_{(k)}) < r_c \text{ for all } 0 \leq t' \leq t, \\ 0 & \text{otherwise.} \end{cases} \quad (70)$$

The critical value, r_c , can be determined by equating the amount of energy required to remove all of the micropotentials across a unit crack surface to the critical energy release rate, $G_{\text{III}C}$, for the mode III type of loading of linear elastic fracture mechanics (LEFM). In order to create a new crack surface, A , all of the micropotentials (interactions) between the material points $\mathbf{x}_{(k^+)}$ and $\mathbf{x}_{(j^-)}$ whose line of action crosses this new surface must be terminated, as sketched in Figure 8. The material points $\mathbf{x}_{(k^+)}$ and $\mathbf{x}_{(j^-)}$ are located above and below the new crack surface, respectively.

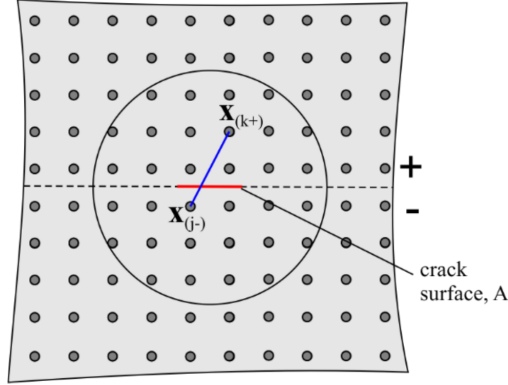


Figure 8. Interaction of the material points $\mathbf{x}_{(k+)}$ and $\mathbf{x}_{(j-)}$ above and below the crack surface.

Hence, the strain energy required to remove the interaction between two material points $\mathbf{x}_{(k+)}$ and $\mathbf{x}_{(j-)}$ can be expressed as

$$W_{(k+)(j-)}^c = \frac{1}{2} \frac{w_{(k+)(j-)}^c + w_{(j-)(k+)}^c}{2} V_{(k+)} V_{(j-)}. \quad (71)$$

Furthermore, the total strain energy required to remove all of the interactions across the newly created crack surface A can be obtained as

$$W^c = \frac{1}{2} \sum_{k=1}^{K^+} \frac{1}{2} \sum_{j=1}^{J^-} w_{(k+)(j-)}^c V_{(k+)} V_{(j-)} + \frac{1}{2} \sum_{k=1}^{K^+} \frac{1}{2} \sum_{j=1}^{J^-} w_{(j-)(k+)}^c V_{(j-)} V_{(k+)}, \quad (72)$$

for which the line of interaction defined by $\xi_{(k+)(j-)} = |\mathbf{x}_{(k+)} - \mathbf{x}_{(j-)}|$ and the crack surface intersect, and K^+ and J^- indicate the number of material points above and below the crack surface within the families of $\mathbf{x}_{(k+)}$ and $\mathbf{x}_{(j-)}$, respectively. If this line of interaction and crack surface intersect at the crack tip, only half of the critical micropotential is considered in the summation.

Considering only the pairwise interactions between $\mathbf{x}_{(k+)}$ and $\mathbf{x}_{(j-)}$ crossing the crack surface, the micropotentials for linear elastic deformation are given by (42) as

$$w_{(k+)(j-)} = \frac{1}{2} c \xi_{(k+)(j-)} r_{(k+)(j-)}^2 \quad \text{and} \quad w_{(j-)(k+)} = \frac{1}{2} c \xi_{(j-)(k+)} r_{(j-)(k+)}^2. \quad (73)$$

Their critical values can be expressed as

$$w_{(k+)(j-)}^{\text{cr}} = \frac{1}{2} c \xi_{(k+)(j-)} r_c^2 \quad \text{and} \quad w_{(j-)(k+)}^{\text{cr}} = \frac{1}{2} c \xi_{(j-)(k+)} r_c^2. \quad (74)$$

Thus, the total strain energy required to remove all of the interactions across the newly created crack surface A becomes

$$W^c = \frac{1}{2} c r_c^2 \sum_{k=1}^{K^+} \sum_{j=1}^{J^-} \xi_{(j-)(k+)} V_{(k+)} V_{(j-)}. \quad (75)$$

The amount of energy required to remove all of the interactions (micropotentials) across the unit crack surface equals the critical strain energy release rate, thus leading to

$$G_{IIIc} = \frac{W^c}{A} = \frac{\frac{1}{2}cr_c^2 \sum_{k=1}^{K^+} \sum_{j=1}^{J^-} \xi_{(j^-)(k^+)} V_{(k^+)} V_{(j^-)}}{A}. \quad (76)$$

As given by Madenci and Oterkus [2014], the summation in (76) can be evaluated as

$$\frac{\sum_{k=1}^{K^+} \sum_{j=1}^{J^-} \xi_{(j^-)(k^+)} V_{(k^+)} V_{(j^-)}}{A} = \frac{h\delta^4}{2}. \quad (77)$$

Thus, the critical shear angle can be obtained as

$$r_c = \sqrt{\frac{2\pi G_{IIIc}}{3\mu\delta}}. \quad (78)$$

The local damage at a point is defined as the weighted ratio of the number of eliminated interactions to the total number of initial interactions of a material point with its family members [Silling and Askari 2005]:

$$\phi(x_{(k)}, t) = 1 - \frac{\sum_{j=1}^N H(t, x_{(j)} - x_{(k)}) V_{(j)}}{\sum_{j=1}^N V_{(j)}}. \quad (79)$$

If the local damage value has a value equal to or larger than 0.5, it can be interpreted as the creation of new crack surfaces.

8. Numerical results

The solution to the PD field equations requires time and spatial integrations while considering constraints and/or loading conditions, as well as initial conditions. The spatial integration is performed by using a Gaussian integration (meshless) scheme because of its simplicity, and time integration by using backward and forward difference explicit integration schemes. The horizon size is commonly defined as three times the spacing between the material points. This ratio is established based on numerical experimentation and the spacing between the material points is based on a convergence study. The domain is divided into a uniform grid, with integration or collocation (material) points associated with specific volumes. Associated with a particular material point, the numerical implementation of spatial integration involves the summation of the volumes of material points within its horizon. However, the volume of each material point may not be embedded in the horizon in its entirety, i.e., the material points located near the surface of the horizon may have truncated volumes. As a result, the volume integration over the horizon may be incorrect if the entire volume of each material point is included in the numerical implementation. Therefore, a volume correction factor is necessary to correct for the extra volume, as explained by Madenci and Oterkus [2014]. The steady-state solution to the PD field equation can be achieved by different techniques; however, in this study, an adaptive dynamic relaxation method (ADR) is employed (described in detail by Madenci and Oterkus [2014]).

The capability of the PD theory is demonstrated by considering (1) a square bar under antiplane shear loading, (2) a bimaterial rectangular bar under antiplane shear loading, (3) a square bar with a crack under

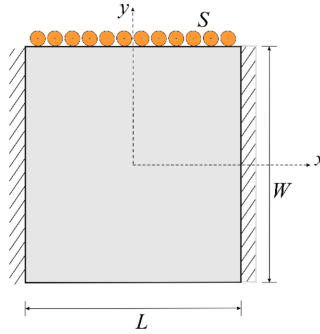


Figure 9. Square bar under antiplane shear loading.

antiplane shear loading, (4) a rectangular bar under torsion, and (5) a rectangular bar with a preexisting crack under torsion. If an analytical solution is not available, a comparison is performed against finite element analysis (FEA) by using ANSYS, a commercially available program, in order to establish the validity of the predictions. During the construction of the solutions to all these problems, uniform spacing, $\Delta x = \Delta y$, between the material points is employed, and the horizon is specified as $\delta = 3.015\Delta x$. Also, the steady-state solutions are achieved by using ADR with a time integration interval of $\Delta t = 1$ s.

8.1. Square bar under antiplane shear loading. As illustrated in Figure 9, a square bar with $L = W = 1$ in is clamped along its left and right surfaces while subjected to a uniform transverse shear stress of $S = 12000$ psi on its top surface. The bottom surface is free of loading. These boundary conditions are imposed as

$$u_z(x = \pm \frac{1}{2}L, y) = 0, \quad \mu \frac{\partial u_z}{\partial y}(x, y = -\frac{1}{2}W) = 0, \quad \mu \frac{\partial u_z}{\partial y}(x, y = \frac{1}{2}W) = S. \quad (80)$$

The shear modulus is specified as $\mu = 12 \times 10^6$ psi. The cross-section is discretized with a uniform grid spacing of $\Delta x = \Delta y = 0.01$ in, resulting in 100 material points in each of the x - and the y -directions. The bond-based and ordinary state-based PD displacement predictions and their comparison with the FEA results are shown in Figure 10. The PD theory successfully captures the antiplane shear deformation, and this comparison confirms the validity of the implementation for displacement- and stress-type boundary conditions.

8.2. Bimaterial rectangular bar under antiplane shear loading. As shown in Figure 11, a bimaterial rectangular bar with $L = 0.2$ in and $W = 1$ in is clamped along its bottom surface and subjected to a uniform transverse shear stress of $S = 12000$ psi on its top surface. The bottom surface is free of any loading. These boundary conditions are imposed as

$$u_z(x, y = -\frac{1}{2}W) = 0, \quad \mu \frac{\partial u_z}{\partial x}(x = \pm \frac{1}{2}L, y) = 0, \quad \mu \frac{\partial u_z}{\partial y}(x, y = \frac{1}{2}W) = S. \quad (81)$$

The shear moduli of the materials are specified as $\mu_1 = 12 \times 10^6$ psi and $\mu_2 = 6 \times 10^6$ psi. The cross-section is discretized with a uniform grid spacing of $\Delta x = \Delta y = 0.01$ in, resulting in 20 and 100 material points in the x - and in the y -directions, respectively.

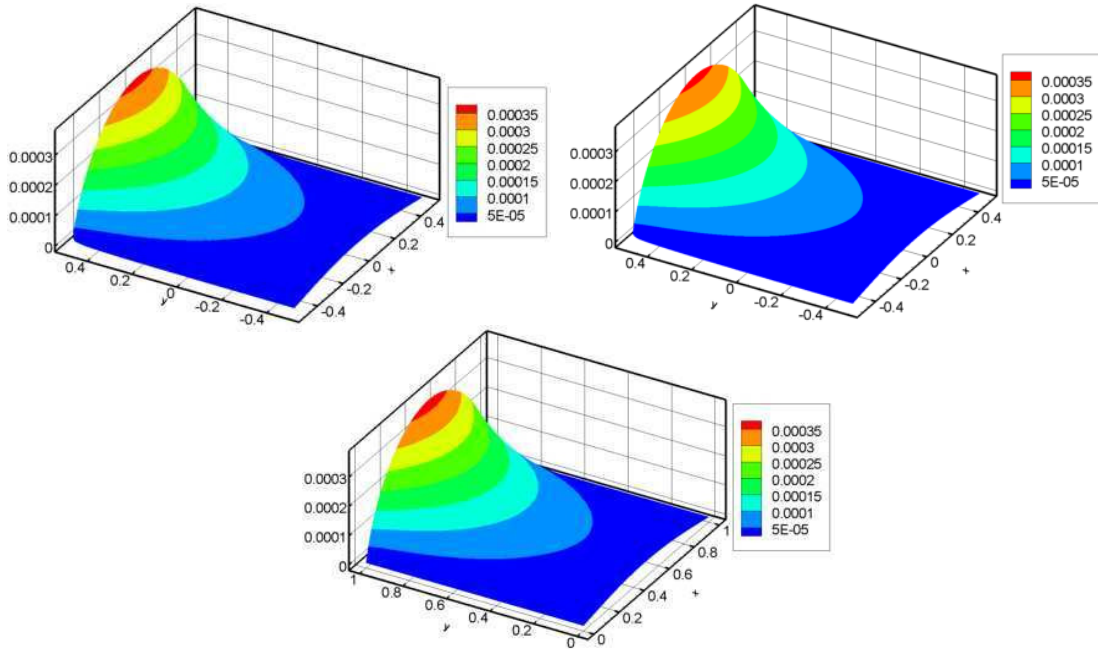


Figure 10. Displacement variation across the bar: (top left) ordinary state-based PD solution, (top right) bond-based PD solution, and (bottom) FEA solution.

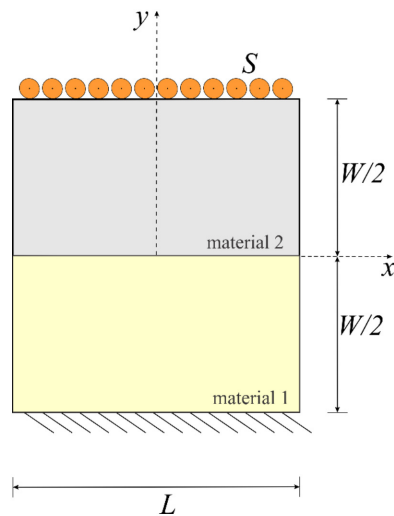


Figure 11. Square bar under antiplane shear loading.

Along the vertical axis, the bond-based and ordinary state-based PD displacement variations and their comparison with the FEA results are shown in Figure 12. The results demonstrate the validity of the PD modeling of interface conditions. The predictions are in excellent agreement and capture the effect of dissimilar materials.

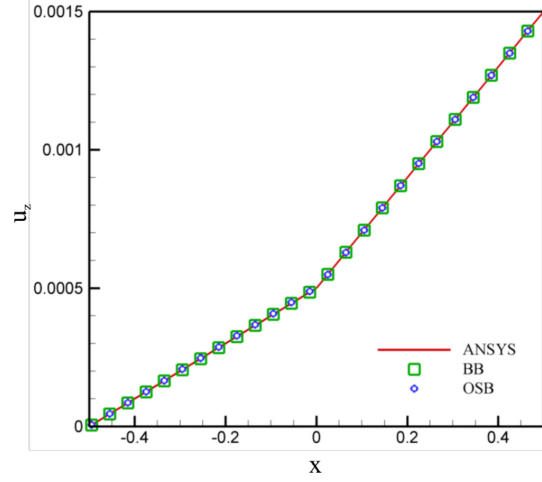


Figure 12. Displacement variation along the vertical axis.

8.3. Square bar with a crack under antiplane shear loading. As illustrated in Figure 13, a square bar with $L = W = 1$ in with a preexisting central crack of length $a = 0.2$ in is subjected to a uniform transverse shear stress of $S = 12000$ psi on its top and bottom surfaces. It is free of any loading and constraints on its other surfaces. These boundary conditions are imposed as

$$\mu \frac{\partial u_z}{\partial x}(x = \pm \frac{1}{2}L, y) = 0, \quad \mu \frac{\partial u_z}{\partial y}(x, y = \frac{1}{2}W) = S, \quad \mu \frac{\partial u_z}{\partial y}(x, y = -\frac{1}{2}W) = -S. \quad (82)$$

The shear modulus is specified as $\mu = 12 \times 10^6$ psi. The critical angle value is specified as $r_{cr} = 0.0035$. The cross-section is discretized with a uniform grid spacing of $\Delta x = \Delta y = 0.01$ in, resulting in 100 material points in both the x - and in the y -directions. As expected, a self-similar crack growth, shown in Figure 14 (left), is observed. Also, the crack surfaces exhibit a tearing type of deformation, as shown in Figure 14 (right).

8.4. Rectangular bar under torsion. As illustrated in Figure 15, a rectangular bar with $L = 1$ in and $W = 2$ in is subjected to a unit angle of twist, $\theta = 1$ in/in. All surfaces of the bar are free of loading. These boundary conditions are

$$\tau_{xz}(x = \pm \frac{1}{2}L, y) = \mu \left[\frac{\partial u_z}{\partial x}(x = \pm \frac{1}{2}L, y) - \theta(y - y_0) \right] = 0 \quad (83)$$

and

$$\tau_{yz}(x, y = \pm \frac{1}{2}W) = \mu \left[\frac{\partial u_z}{\partial y}(x, y = \pm \frac{1}{2}W) + \theta(x - x_0) \right] = 0. \quad (84)$$

They can be rewritten as

$$\frac{\partial u_z}{\partial x}(x = \pm \frac{1}{2}L, y) = \frac{\theta(y - y_0)}{\mu} \quad (85)$$

and

$$\frac{\partial u_z}{\partial y}(x, y = \pm \frac{1}{2}W) = -\frac{\theta(x - x_0)}{\mu}, \quad (86)$$

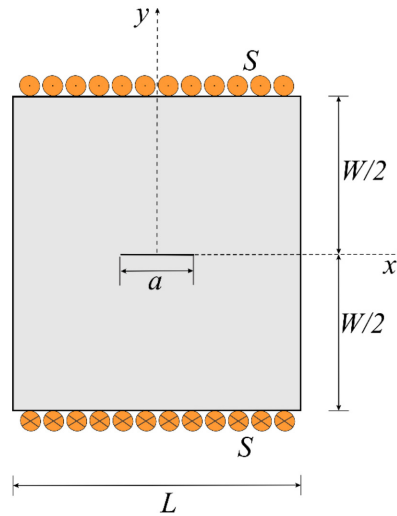


Figure 13. Square bar with a crack under antiplane shear loading.

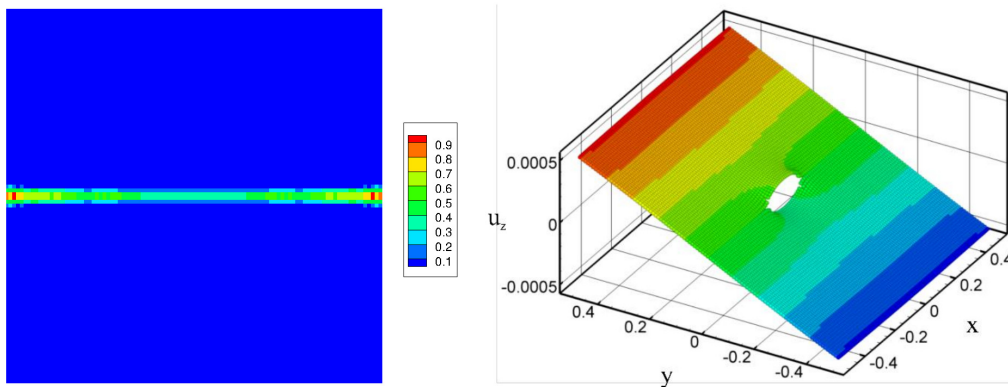


Figure 14. Square bar with a crack under antiplane shear loading: (left) crack growth path (damage distribution), and (right) crack opening mode.

in which x_0 and y_0 represent the coordinates of the reference point on the boundary and are specified as $(0, 0)$. The cross-section is discretized with a uniform grid spacing of $\Delta x = \Delta y = 0.02$ in, resulting in 50 and 100 material points in the x - and in the y -directions, respectively.

The bond-based and ordinary state-based PD warpage predictions and their comparison with the FEA results are shown in Figure 16. Comparisons of the stress predictions are shown in Figures 17 and 18. As shown in these figures, the agreement is remarkable, and the traction-free boundary conditions are enforced through fictitious regions. The PD results capture the expected warping behavior.

8.5. Rectangular bar with a preexisting crack under torsion. The rectangular bar has a preexisting edge crack length of a , as shown in Figure 19. The crack length is varied from 0 to b , as investigated by Armero [2012]. The external boundary conditions and loading are the same as those of the previous

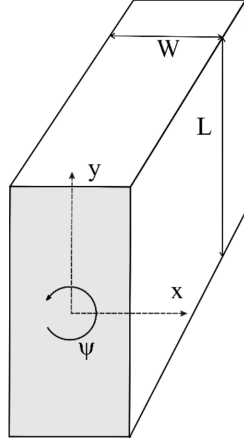


Figure 15. Rectangular bar under torsion.

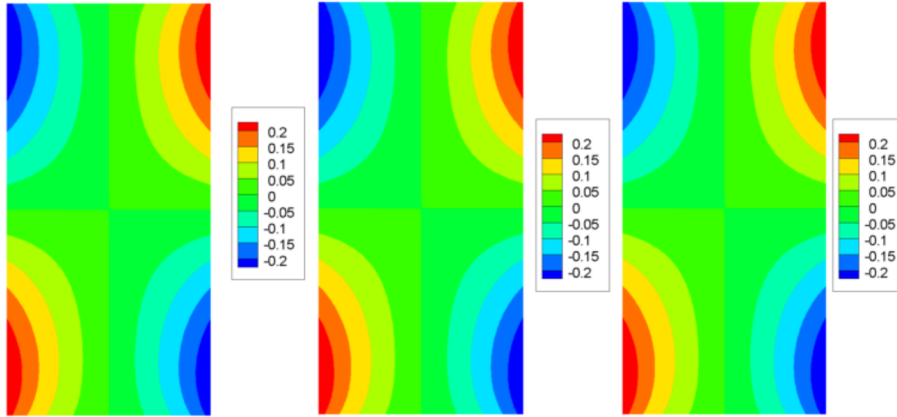


Figure 16. Displacement variation: (left) bond-based solution, (middle) ordinary state-based solution, and (right) exact solution.

problem. The traction-free conditions on the crack surfaces are also imposed explicitly as

$$\tau_{yz}(x, y = \pm 0) = \mu \left[\frac{\partial u_z}{\partial y}(x, y = \pm 0) + \theta(x - x_0) \right] = 0 \quad (87)$$

or

$$\frac{\partial u_z}{\partial y}(x, y = \pm 0) = -\frac{\theta(x - x_0)}{\mu}. \quad (88)$$

The cross-section is discretized with a uniform grid spacing of $\Delta x = \Delta y = 0.005$ in, resulting in 200 and 400 material points in the x - and in the y -directions, respectively.

The bond-based and ordinary state-based PD predictions for the shear stress norm for varying crack lengths are shown in Figures 20 and 21, respectively. These predictions are in remarkable agreement with the results of Armero [2012], who employs finite elements with embedded discontinuities. Figure 22

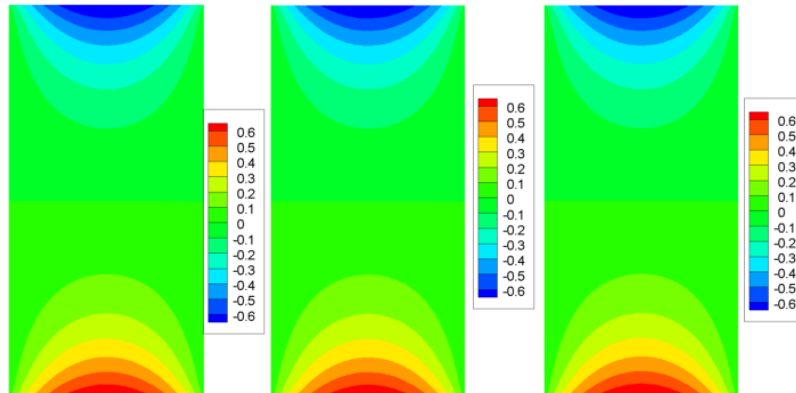


Figure 17. Shear stress, τ_{xz} , variation: (left) bond-based solution, (middle) ordinary state-based solution, and (right) exact solution.

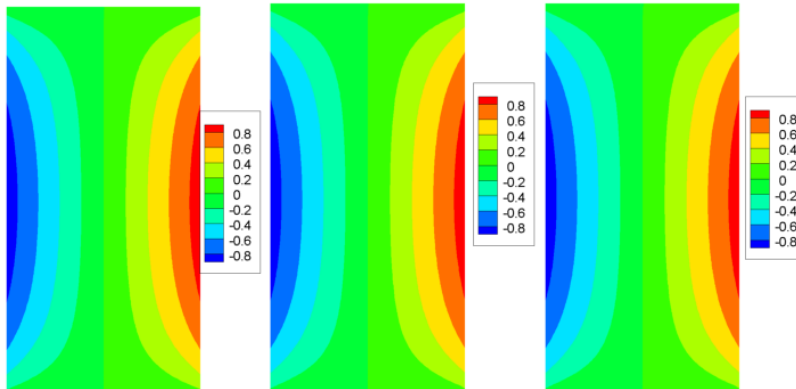


Figure 18. Shear stress, τ_{yz} , variation: (left) bond-based solution, (middle) ordinary state-based solution, and (right) exact solution.

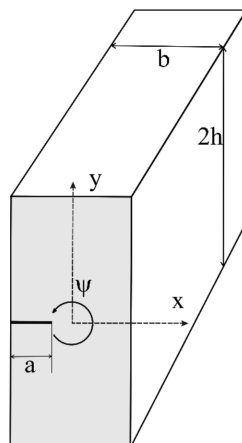


Figure 19. Rectangular bar with a preexisting crack under torsion.

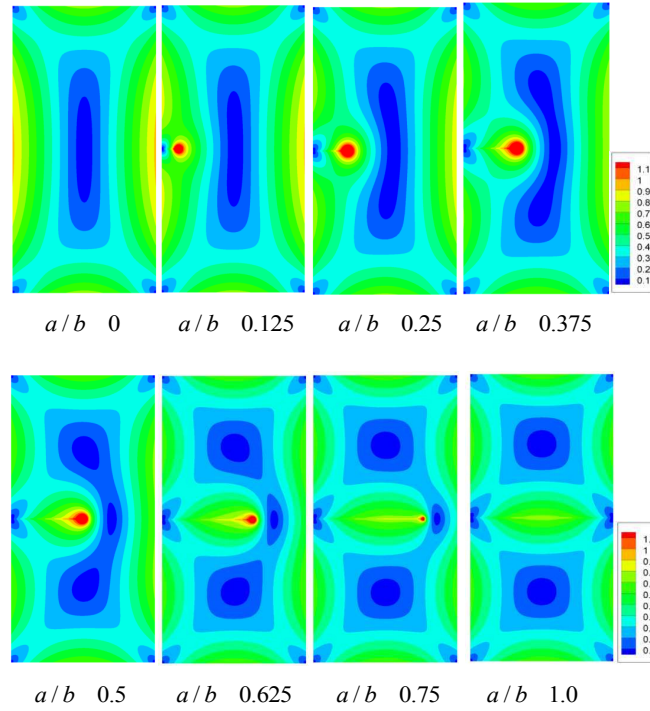


Figure 20. Bond-based PD predictions for stress norm $\tau = \sqrt{\tau_{xz}^2 + \tau_{yz}^2}$.

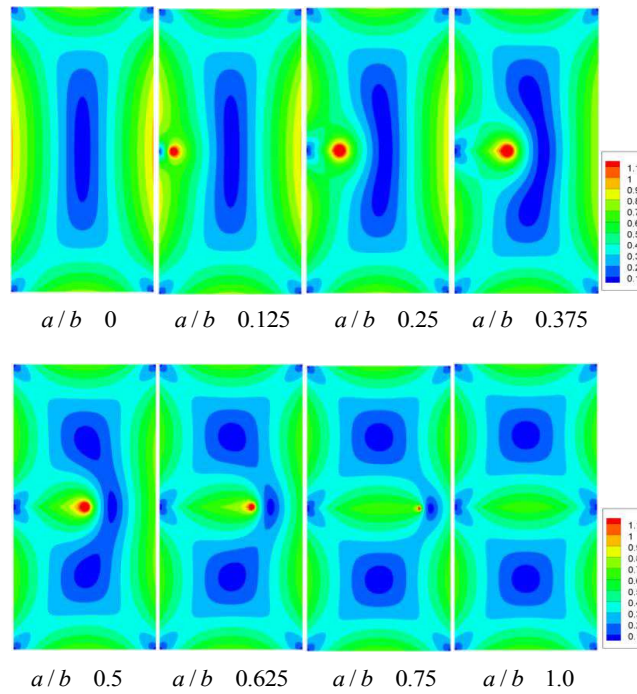


Figure 21. Ordinary state-based PD predictions for stress norm $\tau = \sqrt{\tau_{xz}^2 + \tau_{yz}^2}$.

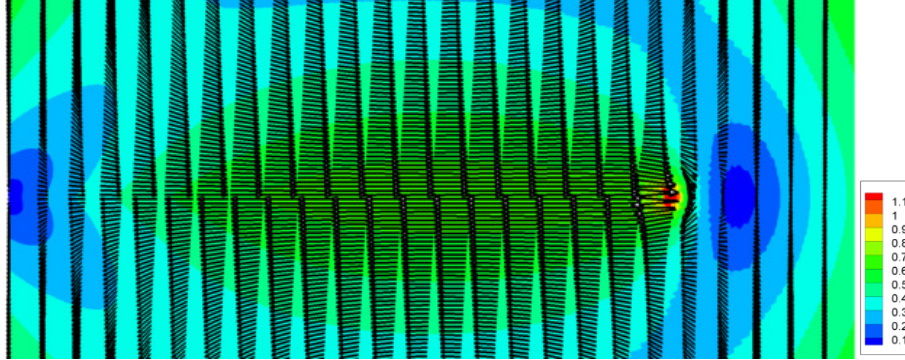


Figure 22. Ordinary state-based PD predictions for stress vector $\boldsymbol{\tau} = \{\tau_{xz}, \tau_{yz}\}$ close to the crack surface for $a/b = 0.75$.

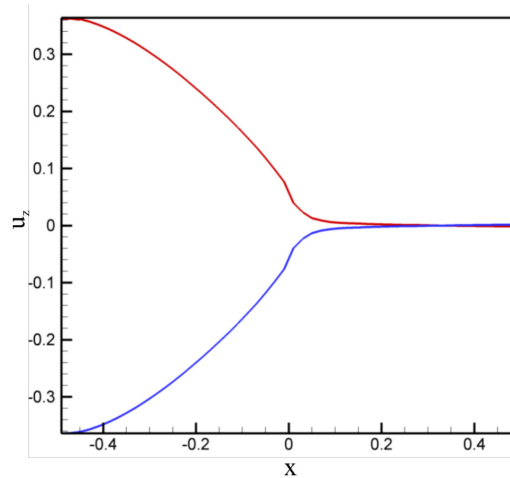


Figure 23. Crack tip opening profile at the crack surface for $a/b = 0.5$.

presents the variation of stress vectors near the crack. As expected, the results show that the stress vectors are aligned with the crack ($\tau_{yz} = 0$). Also, the crack opening displacement is shown in Figure 23. The PD analysis predicts a cusp-like crack opening displacement near the crack tip. It is similar to that obtained by Silling [2000].

9. Final remarks

The classical equilibrium equations for antiplane shear and torsional deformations present only one engineering constant; i.e., shear modulus. Therefore, bond-based peridynamics does not suffer from the loss of an independent engineering constant as in the case of in-plane deformation with a constraint on the Poisson's ratio being $\frac{1}{3}$. If the degree of nonlocality is insignificant, then both the ordinary state-based and bond-based peridynamics lead to the same predictions. However, if the degree of interaction among the material points needs to be specified, then the ordinary state-based peridynamics may be better

suited, such as in the case of a porous medium with fluid pressure. This study describes the determination of the PD material parameters for both formulations, as well as their correction near the free surfaces and interface of dissimilar materials. Inherent with the nonlocal formulations, the imposition of the boundary conditions requires volume constraints. This study also describes the implementation of the essential and natural boundary conditions. The validity of the equations of motion for both ordinary state-based and bond-based peridynamics, the surface correction procedure, and implementation of the boundary conditions are established by considering benchmark problems with complex geometry and boundary conditions. Comparison of the PD predictions with the FEA results proves the fidelity of the peridynamics, which offers its distinct advantage for predicting damage paths.

References

- [Agwai et al. 2011] A. Agwai, I. Guven, and E. Madenci, “Predicting crack propagation with peridynamics: A comparative study”, *Int. J. Fract.* **171**:1 (2011), 65–78.
- [Armero 2012] F. Armero, “Strong discontinuities in antiplane/torsional problems of computational failure mechanics”, *Int. J. Fract.* **178**:1–2 (2012), 3–32.
- [Kilic 2008] B. Kilic, *Peridynamic theory for progressive failure prediction in homogeneous and heterogeneous materials*, Ph.D. thesis, The University of Arizona, 2008, Available at <http://hdl.handle.net/10150/193658>.
- [Lipton 2014] R. Lipton, “Dynamic brittle fracture as a small horizon limit of peridynamics”, *J. Elasticity* **117**:1 (2014), 21–50.
- [Macek and Silling 2007] R. W. Macek and S. A. Silling, “Peridynamics via finite element analysis”, *Finite Elem. Anal. Des.* **43**:15 (2007), 1169–1178.
- [Madenci and Oterkus 2014] E. Madenci and E. Oterkus, *Peridynamic theory and its applications*, Springer, New York, 2014.
- [Oterkus et al. 2014] S. Oterkus, E. Madenci, and A. Agwai, “Peridynamic thermal diffusion”, *J. Comput. Phys.* **265** (2014), 71–96.
- [Silling 2000] S. A. Silling, “Reformulation of elasticity theory for discontinuities and long-range forces”, *J. Mech. Phys. Solids* **48**:1 (2000), 175–209.
- [Silling and Askari 2005] S. A. Silling and E. Askari, “A meshfree method based on the peridynamic model of solid mechanics”, *Comput. Struct.* **83**:17–18 (2005), 1526–1535.
- [Silling and Lehoucq 2010] S. A. Silling and R. B. Lehoucq, “Peridynamic theory of solid mechanics”, pp. 73–168 in *Advances in applied mechanics*, edited by H. Aref and E. van der Giessen, *Advances in applied mechanics* **44**, Elsevier, New York, 2010.
- [Silling et al. 2007] S. A. Silling, M. Epton, O. Weckner, J. Xu, and E. Askari, “Peridynamic states and constitutive modeling”, *J. Elasticity* **88**:2 (2007), 151–184.

Received 3 Feb 2015. Revised 19 May 2015. Accepted 9 Jun 2015.

SELDA OTERKUS: seldaalpay@gmail.com

Department of Aerospace and Mechanical Engineering, The University of Arizona, 1130 N Mountain, Tucson, AZ 85721-0119, United States

ERDOGAN MADENCI: madenci@email.arizona.edu

Department of Aerospace and Mechanical Engineering, The University of Arizona, 1130 N Mountain, Tucson, AZ 85721-0119, United States

JOURNAL OF MECHANICS OF MATERIALS AND STRUCTURES

msp.org/jomms

Founded by Charles R. Steele and Marie-Louise Steele

EDITORIAL BOARD

ADAIR R. AGUIAR University of São Paulo at São Carlos, Brazil
KATIA BERTOLDI Harvard University, USA
DAVIDE BIGONI University of Trento, Italy
YIBIN FU Keele University, UK
IWONA JASIUK University of Illinois at Urbana-Champaign, USA
C. W. LIM City University of Hong Kong
THOMAS J. PENCE Michigan State University, USA
DAVID STEIGMANN University of California at Berkeley, USA

ADVISORY BOARD

J. P. CARTER University of Sydney, Australia
D. H. HODGES Georgia Institute of Technology, USA
J. HUTCHINSON Harvard University, USA
D. PAMPLONA Universidade Católica do Rio de Janeiro, Brazil
M. B. RUBIN Technion, Haifa, Israel

PRODUCTION production@msp.org

SILVIO LEVY Scientific Editor

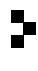
Cover photo: Ev Shafir

See msp.org/jomms for submission guidelines.

JoMMS (ISSN 1559-3959) at Mathematical Sciences Publishers, 798 Evans Hall #6840, c/o University of California, Berkeley, CA 94720-3840, is published in 10 issues a year. The subscription price for 2015 is US\$565/year for the electronic version, and \$725/year (+\$60, if shipping outside the US) for print and electronic. Subscriptions, requests for back issues, and changes of address should be sent to MSP.

JoMMS peer-review and production is managed by EditFLOW® from Mathematical Sciences Publishers.

PUBLISHED BY

 **mathematical sciences publishers**
nonprofit scientific publishing

<http://msp.org/>

© 2015 Mathematical Sciences Publishers

Journal of Mechanics of Materials and Structures

Volume 10, No. 2

March 2015

- On the vibration simulation of submerged pipes: Structural health monitoring aspects** PEJMAN RAZI and FARID TAHERI 105
- Nonuniqueness and instability of classical formulations of nonassociated plasticity I: Case study** THOMAS PUČIK, REBECCA M. BRANNON and JEFFREY BURGHARDT 123
- Nonuniqueness and instability of classical formulations of nonassociated plasticity II: Effect of nontraditional plasticity features on the Sandler–Rubin instability** JEFFREY BURGHARDT and REBECCA M. BRANNON 149
- Peridynamics for antiplane shear and torsional deformations** SELDA OTERKUS and ERDOGAN MADENCI 167
- A hysteretic Bingham model for MR dampers to control cable vibrations** SELSEBIL SOLTANE, SAMI MONTASSAR, OTHMAN BEN MEKKI and RACHED EL FATMI 195



1559-3959(2015)10:2;1-B